AMIDR: A Complete Pulse Method for Measuring Cathode Solid-State Diffusivity

Supporting Information

Mitchell Ball[1], Marc Cormier[2], Eniko Zsoldos[1], Ines Haman[2], Svena Yu[3], Ning Zhang[2], Nutthaphon Phattharasupakun[2,4], Michel B. Johnson[2], Michael Metzger[1,2], Chongyin Yang[1,2], and Jeff Dahn[1,2,z]

[1] Department of Chemistry, Dalhousie University, Halifax, Nova Scotia B3H 4R2, Canada

[2] Department of Physics and Atmospheric Science, Dalhousie University, Halifax, Nova Scotia B3H 4R2, Canada

[3] Department of Process Engineering and Applied Science, Dalhousie University, Halifax, Nova Scotia B3H 3J5, Canada

[4] Department of Chemical and Biomolecular Engineering, School of Energy Science and Engineering, Vidyasirimedhi Institute of Science and Technology, Rayong 21210, Thailand

[z] Corresponding author – Jeff.Dahn@dal.ca

14 **Proofs**

15 *Proof S1: Start of Pulse Bound for an Ensemble of Geometries with Varying Diffusion Length*

16   For pulses that stop near their start, flux is uniform for both small and large geometries.

17 Using equation 6 and the definitions $Q = \Delta q_{tot} I^{-1} D_c r^{-2}$ and $\tau = \Delta q / \Delta q_{tot}$ returns an equation

18 for calculating the Δq_{tot} for a single geometry that has stopped its pulse near its start,

19
$$\Delta q_{tot} = \frac{2r\sqrt{I\Delta q}}{A\sqrt{\pi D_c}}.$$
(S1)

20 Accordingly, the Δq_{tot} for multiple geometries that have stopped their pulse near its start is

21 calculated as

22
$$\Delta q_{tot} = \sum \Delta q_{tot,j} = \sum \left(\frac{2r_j\sqrt{I_j\Delta q_j}}{A\sqrt{\pi D_c}} \right) = \frac{2\sum r_j\sqrt{I_j\Delta q_j}}{A\sqrt{\pi D_c}}.$$
(S2)

23 where the j subscript is given for individual geometries. As flux is uniform near the start of a

24 pulse, the I_j and Δq_j per geometry is proportional to a geometry's S_j, and therefore a geometry's

25 r_j^2 as

26
$$I_j = \frac{IS_j}{\sum S_j} = \frac{Ir_j^2}{\sum r_j^2}, \text{ and}$$
(S3)

27
$$\Delta q_j = I_j \Delta t = \frac{I \Delta t r_j^2}{\sum r_j^2} = \frac{\Delta q r_j^2}{\sum r_j^2}.$$
(S4)

28 Entering these into equation S2 gives

29
$$\Delta q_{tot} = \frac{2\sqrt{I\Delta q} \sum r_j^3}{A\sqrt{\pi D_c} \sum r_j^2}.$$
(S5)

      S2

30   Defining $\bar{r}_s = \sum r_j^3 / \sum r_j^2$ returns equation S1. Therefore, $\bar{r}_s$ averaged in this manner will

31   accurately define the bound for pulses that stop near the start of the pulse.

32   *Proof S2: End of Pulse Bound for an Ensemble of Geometries with Varying Diffusion Length*

33   For pulses that stop near their end, flux is proportional to a geometry's $\tilde{V}/S$. Using

34   equation 7 and the definitions $Q = \Delta q_{tot} I^{-1} D_c r^{-2}$ and $\tau = \Delta q / \Delta q_{tot}$ returns an equation for

35   calculating the Δq_{tot} for a single geometry that has stopped its pulse near its end,

$$36 \qquad\qquad \Delta q_{tot} = \Delta q + \frac{I r^2}{ABD_c}. \qquad\qquad (S6)$$

37   Accordingly, the Δq_{tot} for multiple geometries that have stopped their pulse near its end is

38   calculated as

$$39 \qquad \Delta q_{tot} = \sum \Delta q_{tot,j} = \sum \left(\Delta q_j + \frac{I_j r_j^2}{ABD_c} \right) = \Delta q + \frac{\sum I_j r_j^2}{ABD_c}. \qquad (S7)$$

40   where the j subscript is given for individual geometries. As flux is proportional to a geometry's

41    $\tilde{V}/S$ near the end of a pulse, the I_j per geometry is proportional to a geometry's $\tilde{V}_j$, and therefore

42   a geometry's r_j^3 as

$$43 \qquad\qquad I_j = \frac{I \tilde{V}_j}{\sum \tilde{V}_j} = \frac{I r_j^3}{\sum r_j^3}. \qquad\qquad (S8)$$

44   Entering this into equation S7 gives

$$45 \qquad\qquad \Delta q_{tot} = \Delta q + \frac{I \sum r_j^5}{ABD \sum r_j^3}. \qquad\qquad (S9)$$

S3

46   Defining $\bar{r}_e = \left(\sum r_j^5 / \sum r_j^3 \right)^{1/2}$ returns equation S6. Therefore, $\bar{r}_e$ averaged in this manner will

47   accurately define the bound for pulses that stop near the end of the pulse.

48   *Proof S3: Impedance of a Thin, Low Diffusivity Surface Layer*

49   A more complete form of equation 3 showing X in the interior of the geometry is

50     $$X(\tau) = \tau + \frac{1}{AQ}\left(\frac{1}{B} + \frac{y^2}{2} - \frac{1}{2} - 2\sum_{i=1}^{\infty} \frac{e^{-\alpha_i^2 Q\tau}}{\alpha_i^2} C(\alpha_i, y) \right), \qquad (S10)$$

51   where the ascending, non-zero series α_i and function $C(\alpha_i, y)$ are defined for each geometry as

52   Planar Sheet: $\sin(\alpha) = 0 \; \{\alpha_1 = \pi, \alpha_2 = 2\pi, \dots \}$,

53     $$C(\alpha, y) = \frac{\cos(\alpha y)}{\cos(\alpha)},$$

54   Cylinder: $J_1(\alpha) = 0$,

55     $$C(\alpha, y) = \frac{J_0(\alpha y)}{J_0(\alpha)},$$

56   Sphere: $\alpha\cot(\alpha) - 1 = 0$,

57     $$C(\alpha, y) = \frac{\sin(\alpha y)}{y \sin(\alpha)},$$

58   y is the relative position along the diffusion path on a scale from 0, the center, to 1, the surface,

59   and J_0 is the Bessel function of the first kind of order 0.[1] Taking the derivative of X in terms of y

60   returns

61     $$\frac{dX(\tau)}{dy} = \frac{1}{AQ}\left(y - 2\sum_{i=1}^{\infty} \frac{e^{-\alpha_i^2 Q\tau}}{\alpha_i^2} \frac{dC(\alpha_i, y)}{dy} \right), \qquad (S11)$$

62   where the ascending, non-zero series α_i and function $C(\alpha_i, y)$ is defined for each geometry as

63   Planar Sheet: $\sin(\alpha) = 0 \; \{\alpha_1 = \pi, \alpha_2 = 2\pi, \dots \}$,

          S4

64
$$\frac{dC(\alpha, y)}{dy} = -\frac{\alpha \sin(\alpha y)}{\cos(\alpha)},$$

65   Cylinder: $\qquad\qquad\qquad J_1(\alpha) = 0,$

66
$$\frac{dC(\alpha, y)}{dy} = -\frac{\alpha J_1(\alpha y)}{J_0(\alpha)},$$

67   Sphere: $\qquad\qquad\qquad \alpha\cot(\alpha) - 1 = 0,$

68
$$\frac{dC(\alpha, y)}{dy} = \frac{\alpha y \cos(\alpha y) - \sin(\alpha y)}{y^2 \sin(\alpha)}.$$

69   Next, the derivative of X in terms of y near the surface is calculated as

70
$$\lim_{y \to 1} \frac{dX(\tau)}{dy} = \frac{1}{AQ}\left(1 - 2\sum_{i=1}^{\infty} \frac{e^{-\alpha_i^2 Q\tau}}{\alpha_i^2} \lim_{y \to 1} \frac{dC(\alpha_i, y)}{dy}\right), \qquad\qquad \text{(S12)}$$

71   where the ascending, non-zero series α_i and function $C(\alpha_i, y)$ is defined for each geometry as

72   Planar Sheet: $\qquad\qquad \sin(\alpha) = 0 \; \{\alpha_1 = \pi, \alpha_2 = 2\pi, \dots\},$

73
$$\lim_{y \to 1} \frac{dC(\alpha_i, y)}{dy} = -\alpha \tan(\alpha) = 0,$$

74   Cylinder: $\qquad\qquad\qquad J_1(\alpha) = 0,$

75
$$\lim_{y \to 1} \frac{dC(\alpha_i, y)}{dy} = -\frac{\alpha J_1(\alpha)}{J_0(\alpha)} = 0,$$

76   Sphere: $\qquad\qquad\qquad \alpha\cot(\alpha) - 1 = 0,$

77
$$\lim_{y \to 1} \frac{dC(\alpha_i, y)}{dy} = \alpha \cot(\alpha) - 1 = 0.$$

78   Conveniently, under these specific conditions $\lim_{y \to 1} \frac{dC(\alpha_i, y)}{dy} = 0$ for all geometries. This shows that

79   the change in concentration over diffusion path position near the surface is always simply

80
$$\lim_{y \to 1} \frac{dX}{dy} = \frac{1}{AQ}, \qquad\qquad \text{(S13)}$$

S5

81   for all geometries and all τ. This equation being true for all τ is essential for a thin, low D_c

82   surface layer to act as a resistor independent of time.

83   A thin, low D_c surface layer will generate a relative change in surface concentration, $X_{s,l}$,

84   in addition to the X_s related to the bulk diffusion of the active material. As long as this surface

85   layer is thin enough, $X_{s,l} = \lim_{z \to 1} \frac{dX}{dy} H = \frac{H}{AQ}$ where $H = h/r$ is the relative thickness and h is the

86   thickness (cm) of the surface layer. This can be converted out of dimension-less convention to

87   generate a change in surface concentration at the surface layer, $\Delta c_{s,l}$, as

$$\Delta c_{s,l} = \frac{Irh}{AzF\tilde{V}D_c}. \tag{S14}$$

88

89   Next, this can be converted into a surface layer overpotential, η_l, using dE/dc of the surface

90   layer as

$$\eta_l = -\frac{dE}{dc}\frac{Irh}{AzF\tilde{V}D_c}. \tag{S15}$$

91

92   where positive I is now treated as current driving positive ions to leave the active material, the

93   typical convention for working electrodes. Finally, this overpotential can be treated as a resistor

94   given $V = IR$ to give a surface layer resistance, R_l, as

$$R_l = -\frac{dE}{dc}\frac{rh}{AzF\tilde{V}D_c}. \tag{S16}$$

95

96   Similar to equation 13, this is dependent on both dE/dc and D_c which will be unique to the

97   phase of the surface layer.

98   **Additional List of Symbols**
          S6

99	$\Delta c_{s,l}$	Δc in addition to Δc_s at the surface layer (mol cm^{-3})
100	$C(\alpha, z)$	geometric function
101	h	surface layer thickness (cm)
102	H	relative h
103	I_j	I of an individual particle (A)
104	Δq_j	Δq of an individual particle (C)
105	r_j	r of an individual particle (cm)
106	R_l	surface layer R (Ω)
107	S_j	S of an individual particle (cm^2)
108	$\tilde{V}_j$	$\tilde{V}$ of an individual particle (cm^3)
109	X	relative Δc
110	$X_{s,l}$	X in addition to X_s at the surface layer
111	y	relative position along diffusion path
112	η_l	surface layer η (V)

113 **Experimental**

114 *Scanning Electron Microscopy (SEM) Imaging and Particle Sizing*

115   SEM images were taken with a ThermoFisher Scientific AxiaSEM (USA). The materials

116 were placed onto a conductive carbon tape adhered to a stub for SEM imaging. A Secondary

117 Electron detector was used in high-vacuum mode, and the images were collected at an

118 accelerated voltage of 5 kV and a current of 12 pA.

119   An image containing at least 200 particles such as Figure S1a was selected for each

120 material and the particles were given boundaries by hand with a paintbrush tool. These

121 boundaries are then recognized by a simple image analysis software, ImageJ, and the particles

122 individualized such as in Figure S1b and assigned an area using the scale defined by the SEM.

123 The radii of the particles are then calculated as $r = \sqrt{A/\pi}$ and averaged using the capacity-

124 weighted, geometric mean as $\bar{r} = 10^{\frac{\sum \log r_j * r_j^3}{\sum r_j^3}}$. Additionally, $\bar{r}_s = \sum r_j^3 / \sum r_j^2$ and $\bar{r}_e =$

125    $\left(\sum r_j^5 / \sum r_j^3\right)^{1/2}$ for calculating the start and end bounds considering diffusion length variation

126   are also calculated to check and ensure that the particle size distribution is not too wide. Table S1

127   shows that all active materials analyzed by SEM had relatively similar particle sizes and limited
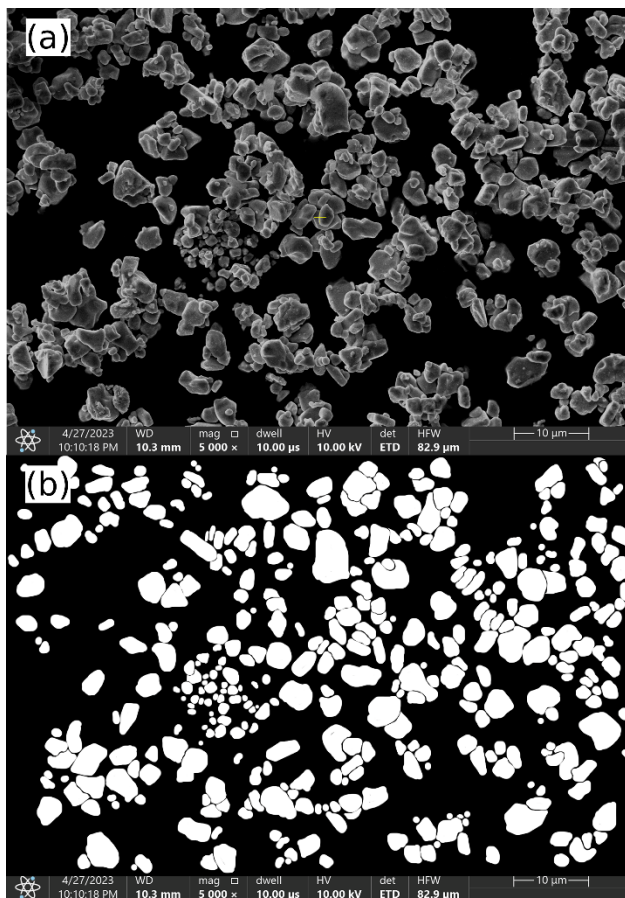
128   size variation.

129

130

131   Figure S1: NMC811 example of a scanning electron microscope (SEM) image (a) before and (b) after
132   particle individualization.

133   Table S1: Results of Particle Size Averaging

Material	$\bar{r}$	$\bar{r}_s$	$\bar{r}_e$	Pulse Start Q-shift $(\bar{r}_s/\bar{r})^2$	Pulse End Q-shift $(\bar{r}_e/\bar{r})^2$
NMC640	0.784 μm	0.737 μm	0.871 μm	0.884	1.23

NMC811	1.736 μm	1.607 μm	1.947 μm	0.857	1.26
NM9505	1.318 μm	1.173 μm	1.596 μm	0.792	1.47

134

135 *Electrode Construction*

136   For low mass loading electrodes, cathode active material (Zhenhua NMC640, Umicore

137 NMC811, Zhenhua NM9505), Super-S carbon black, and polyvinylidene fluoride (PVDF) were

138 combined in a ratio of 84:8:8 by weight. Then, N-methyl-2-pyrrolidone (NMP) was added as a

139 solvent to form a 33% solids weight slurry after mixing in a planetary mixer (Mazerustar) for

140 300 s. The slurries were then coated onto Al foil using a 38 μm notch bar upon a smooth glass

141 plate and dried in an oven at 120 °C for 1 hour, resulting in coatings with partially visible Al foil

142 and mass loadings of $0.6 - 2.4$ mg cm^{-2} depending on the active material used. Next, the

143 electrode sheets were calendared at a pressure of ~2000 atm and punched into 1.275 cm diameter

144 discs.

145 *3-Electrode Coin Cell Assembly*

146   The reference electrode, a 50 μm diameter Au wire with a 7 μm thick polyimide

147 insulation (Goodfellow Cambridge Ltd., United Kingdom), was cut into lengths of $2 - 3$ cm.

148 Each end was then cut or stripped with a scalpel under an optical microscope at 50X. The

149 exterior end was stripped on one side as shown in Figure S2a for a length of ~4 mm to later

150 ensure contact with solder used to connect to a Ni contact tab. The interior end was cut by

151 getting the scalpel underneath the polyimide coating as if to begin stripping and then rotated

152 downward and cut at a $30 - 60°$ angle. This ensured a small interface with the electrolyte without

153 risk of the metallic end being sealed off by the polyimide coating which can happen if just the

154 wire is simply cut at a 90° angle. Then the middle of the wire was secured between a 2325-type

155 coin cell casing top cap clipped to a polypropylene gasket. Next, the cap assembly, coin cell

156 casing bottom can, spacer, spring, and positive electrode were dried in a 110 °C vacuum

157 antechamber overnight before being entered into a glovebox. Inside the glovebox, the coin cell

158 was assembled upside down with the cap assembly first as show in Figure S2b. The negative

159 electrode, a lithium metal foil, was placed in contact with the spacer before being covered by a

160 20 µm separator (Celgard 2300), the interior reference electrode end, 75 µl of 1.5 M $LiPF_6$ in

161 ethylene carbonate (EC):dimethyl carbonate (DMC) electrolyte (1:1 v/v), and another separator

162 in that order. Lastly, the cathode and can were placed on top and the cell crimped and sealed at

163 300 atm pressure with the exterior reference electrode end placed on top of the cap to avoid

164 shearing of the wire. Lastly, after removing from the glovebox, the exterior reference electrode

165 end was soldered into a folded Ni contact tab and covered and protected by dried epoxy (Loctite
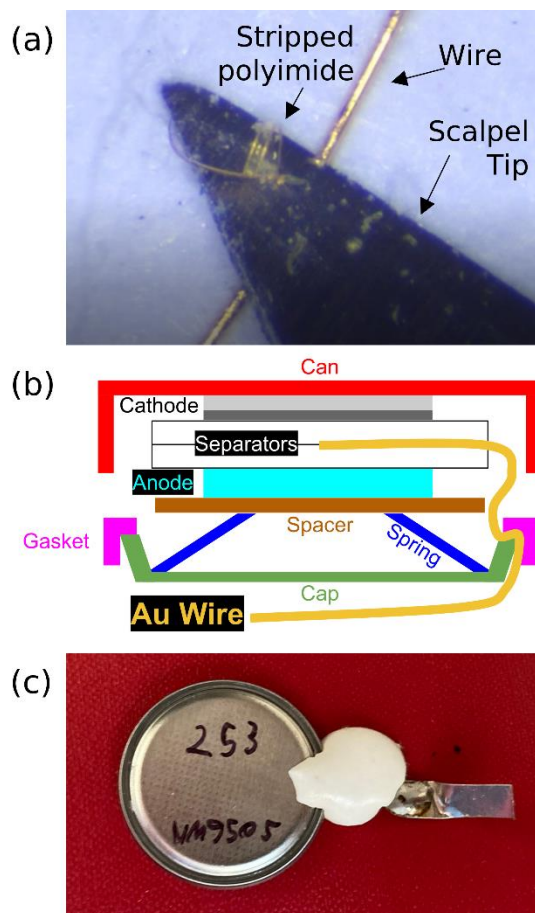
166 EA-1C) as shown in Figure S2c.

Figure S2: Custom reference electrode coin cells. (a) Stripping of the wire under optical microscope with a scalpel, (b) cross section schematic of the 3 electrode coin cell assembly, (c) appearance of a 3 electrode coin cell after epoxy has set.

Reference Electrode Lithiation

The reference electrode was lithiated against the cathode at 150 nA for 1 hour by a BioLogic VMP-3e and allowed to relax for > 1 hour until the reference electrode's potential settled at ~0.31 V vs. Li^+/Li^0. Because I was so small the change in the cathode's SOC was negligible.

Cell and Wire Shielding

Figure S3 shows the steps of the cell shielding arrangement. The BioLogic VMP-3e was selected for AMIDR testing and comes with wires partially shielded by a shielded cable up to ~10 cm near their ends. These wires were attached to a BioLogic CCH-1 4-point connection coin

S11

180   cell holder where the coin cell was held. First, the coin cell holder and all wires except the

181   ground wire were sealed inside a nitrile glove with the open end tied around the shielded cable

182   and the end of the ground wire with a twist tie. The ground wire was then attached to a sheet of

183   aluminum foil which was wrapped entirely around the nitrile glove and tightly sealed around the

184   shielded cable. Then, the aluminum foil was sealed inside a second nitrile glove with the open

185   end again tied around the shielded cable with a twist tie. Lastly, the cells were tested in a metallic

186   temperature box which provided an extra layer of shielding.
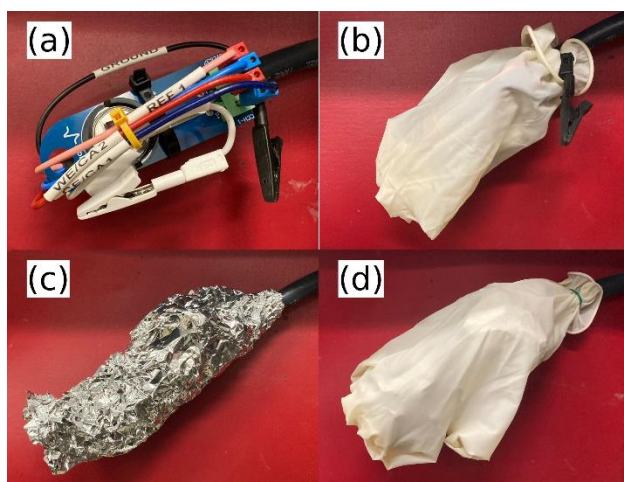
187

188   Figure S3: Shielding steps: (a) Uncovered cell holder wrapped into a tight form factor, (b) cell holder
189   wrapped in a first layer of insulating nitrile glove with ground wire out, (c) cell holder wrapped
190   completely with aluminum foil attached to the ground wire, (d) cell holder wrapped in a second layer of
191   insulating nitrile glove.

AMIDR Protocols

193   All cells began with a 1.5 cycle formation protocol consisting of a C/20 charge to 4.2 V, a

194   C/20 discharge to 3.0 V, another C/20 charge to 4.2 V, and a 15 minute V hold at 4.2 V. After

195   this, pulse protocols were applied with the parameters given by and in the order of Table S2. In

196   between protocols are unrecorded rest steps with longer than the prescribed rest times often up to

197   a day or two. The standard protocol was used for NMC640 and NMC811 materials. The beta

198   protocol was used for NM9505 early in development of AMIDR, but otherwise the high

199   resolution protocol was used for NM9505 to get better detail to compensate for its higher

200   variance dq/dV.

201   Table S2: Pulse Protocol Parameters

Test	Parameters	4.2-3.95 V	3.95-3.7 V	3.7-3.5 V	3.5-3.7 V	3.7-3.95 V	3.95-4.2 V
Standard	V Limit Spacing	25 mV		25 mV	10 mV	25 mV	
	Rate	C/40		C/120	C/300	C/40	
	Rest Time	1 hour		4 hour	4 hour	1 hour	
Beta	V Limit Spacing	25 mV		25 mV	25 mV	25 mV	
	Rate	C/40		C/120	C/120	C/40	
	Rest Time	1 hour		4 hour	4 hour	1 hour	
High Res	V Limit Spacing	12-13 mV	12-13 mV	12-13 mV	10 mV	12-13 mV	12-13 mV
	Rate	C/80	C/80	C/240	C/300	C/80	C/80
	Rest Time	1 hour	1 hour	4 hour	4 hour	1 hour	1 hour

202

203   Table S3 gives some GITT protocol parameters found in published work for comparison

204   to AMIDR. While each protocol is different and performed on a different material some

205   generalities can be determined. Firstly, it is unlikely many complete pulses were obtained given

206   the generally short pulse duration times and the high rates used. Secondly, there does not appear

207   to be any rigorous justification for the relaxation times, so they may not be adequate for every

208   measurement. Lastly, given the larger number of pulses taken and lack of tuning of parameters

209   for different SOC, these tests likely took a lot longer than the typical AMIDR test.

210   Table S3: Common GITT Protocol Parameters[2]

Rate	Pulse Duration Time	Relaxation time
C/10	5 min	2 h
C/20	90 min	5 h
C/10	10 min	40 min

S13

C/10	20 min	2 h
C/20	60 min	4 h
C/5	10 min	40 min
C/20	15 min	45 min
C/10	10 min	2 h
C/10	20 min	1 h
C/10	5 min	1 h
C/10	30 min	2 h
C/20	20 min	2 h
0.4 C	5 min	3 h
C/25	90 min	10 h
C/20	120 min	10 h

211

212   The protocols used are available in the package containing the AMIDR program. These

213   protocols can be lightly modified for different materials, but care should be taken to not disturb a

214   few key elements that are essential to allow the AMIDR program to properly read and analyze

215   the results. Each pulse is composed of a series of CC steps sampling every 0.001 s for 1 s, 0.01 s

216   for 9 s, 0.1 s for 90 s, 1 s for 900s, and 10 s indefinitely. Additional steps could be added to a

217   pulse, but it was not expected that a pulse would last longer than 10,000 s. The AMIDR program

218   automatically averages 100 recorded datapoints together so that each step contributes 9 (or 10 for

219   the first step) high voltage resolution datapoints for analysis. If additional datapoints are

220   recorded, the datapoints would achieve better voltage resolution, but the recorded files would

221   also be larger. Each rest period is composed of a long rest step and two short 0 A CC steps.

222   When a rest step is applied, this means that the galvanometer of the cell tester is physically

223   disconnected, whereas a 0 A CC step means that the galvanometer is connected to the cell, and 0

224   A of current is aimed for, but a small amount of current is still recorded. The rest step is

S14

225   therefore desired to prevent unexpected change in SOC during long rest periods. However, when

226   the galvanometer is reconnected at the transition from a rest step to a CC step, it introduces a

227   small amount of static charge to the cell which can impact the measured voltage. Therefore, two

228   0 A CC steps are included. One to allow the static charge to dissipate, and a second to capture a

229   high resolution relaxed cell voltage before a pulse. The AMIDR program automatically

230   recognizes these different steps and analyzes them accordingly. It's important to note that at the

231   start of the beta protocol the issue with reconnection of galvanometer producing static charge

232   was not realized and the results include unaccounted for ΔV at the beginning of the pulses. This

233   error was fixed at ~4.0 V during discharge, but pulses before this had somewhat erroneous D_c

234   and very erroneous R measured.

235   *AMIDR Analysis Parameters*

236   All cell data was analyzed with the single pulse AMIDR program with default settings.

237   The pulse data analyzed was the measured potential of the active material versus the reference

238   electrode while the results are labeled with the active material potential versus the lithium metal

239   anode. All pulses were fit to the spherical model and used the inputs listed in Table S4 to

240   calculate D_c, Li saturation, and D_t^*. The specific capacities of low mass loading cells are hard to

241   measure due to small and inaccurate active mass measurements and amplified formation side

242   reactions. Therefore, the recorded specific capacities are linearly adjusted to match the specific

243   capacities of regular mass loading cells at certain voltages. The active material density value

244   used to calculate ρ_d was 4.9 g cm^{-3} for all materials as any error in this value is inconsequential

245   on a logarithmic scale.

246   Table S4: Fitting and Calculation Parameters

Material	Radius	Temperature	Theoretical Fully	Regular Loading	Regular Loading

S15

			Desaturated Capacity	**Datapoint 1**		**Datapoint 2**	
NMC640	0.784 μm	303.15 K	279 mAh/g	74 mAh/g	3.8 V	148 mAh/g	4.1 V
NMC811	1.736 μm	303.15 K	275.5 mAh/g	70 mAh/g	3.7 V	178 mAh/g	4.1 V
NM9505	1.318 μm	303.15 K	275 mAh/g	66 mAh/g	3.7 V	149 mAh/g	4.0 V

247

248 *X-ray Diffraction (XRD) and Ni in Li Layer (Ni_{Li}) Calculation*

249   Powder XRD spectra were obtained using a Bruker D8 diffractometer with a Cu target X-

250 ray tube and a diffracted beam monochromator. The spectra were collected over a scattering

251 angle range of 15° to 70° in 0.02° steps at 3 s per step. The lattice parameters and cation-mixing

252 rates were determined from refinements made with the Rietveld structure refinement software

253 Rietica using the R-3m space group. Li was assumed to occupy 3a sites (lithium layer) while the

254 3b sites (metal layer) contained Ni, Mn, and Co and 6c sites contained oxygen. The exchange of

255 Ni and Li between 3a and 3b sites was allowed with the constraint of maintaining the

256 stoichiometry of the material.

257   Powder XRD was accomplished primarily to determine Ni_{Li} to compare to D_c results.

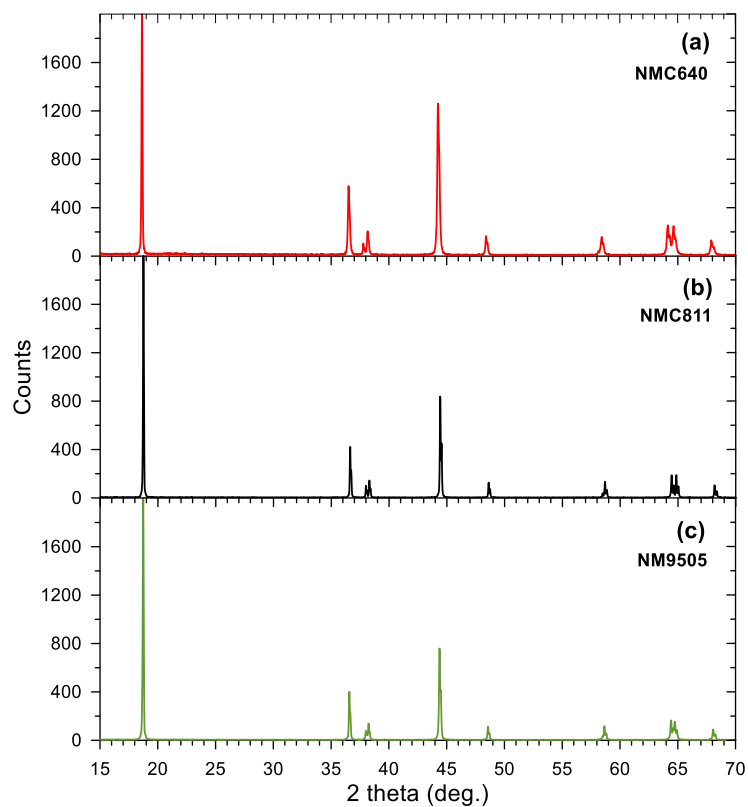258 Figure S4 shows the spectra results and Table S5 shows the results of the Reitveld refinement.

259

Figure S4: XRD Spectra

261

Table S5: Reitveld Refinement

Material	Lattice Parameter a	Error	Lattice Parameter s	Error	%Ni in Li layer	Error	Bragg R-Factor
NMC640	2.8817 Å	6.66E-5 Å	14.264 Å	5.73E-4 Å	7.45%	0.1166%	5.87
NMC811	2.8719 Å	5.78E-5 Å	14.189 Å	2.94E-4 Å	2.20%	0.1431%	3.02
NM9505	2.8766 Å	5.64E-5 Å	14.190 Å	2.81E-4 Å	1.86%	0.1183%	2.72

262

S17

263 **Intermediate Analysis Results**

264   Figure S5 shows an example of a plot that AMIDR first produces after combination of

265 test files from individual protocols. If a test file has been forgotten to be included, it will be

266 apparent in this plot. In addition, AMIDR also produces the plots shown in Figure S6 which

267 show the relaxed potentials of cells undergoing AMIDR in terms of charge vs. discharge. While

268 some cells showed better matching than others, all these cells were considered acceptable.

269
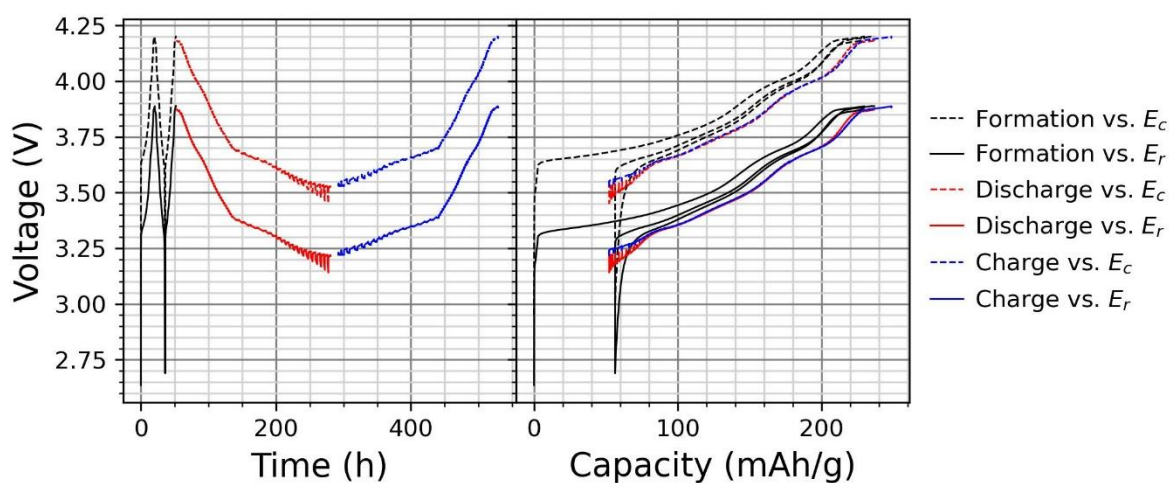
270   Figure S5: Example of complete test summary of a single cell.

271
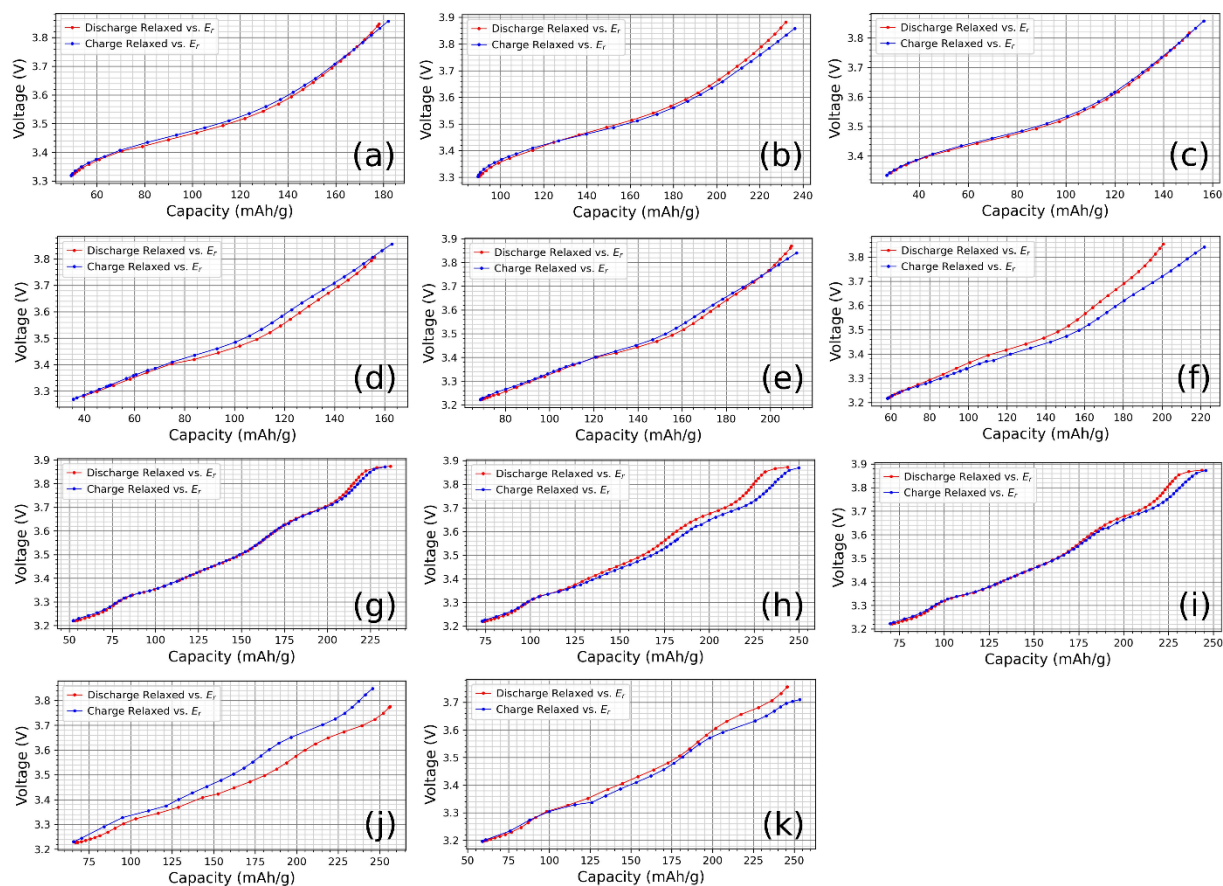
Figure S6: Matching Charge vs. Discharge relaxed potentials of (a-c) NMC640, (d-f) NMC811, (g-i)
NM9505 with high resolution protocol, (j-k) NM9505 with beta protocol.

272
273

274

275   Figure S7 shows fits that were removed due to having too much change in dq/dV and

276   Figure S8 shows fits that were removed due to having too little τ. Out of the remaining fits,

277   Figure S9 shows those with the worst fit error and Figure S10 shows a random sample. Some of

278   the fits with too little τ may look acceptable, however, they began when the active material was

279   not completely relaxed. The worst fitting acceptable fits are not perfect, but they are close

280   enough to give reasonable results.

281

S20
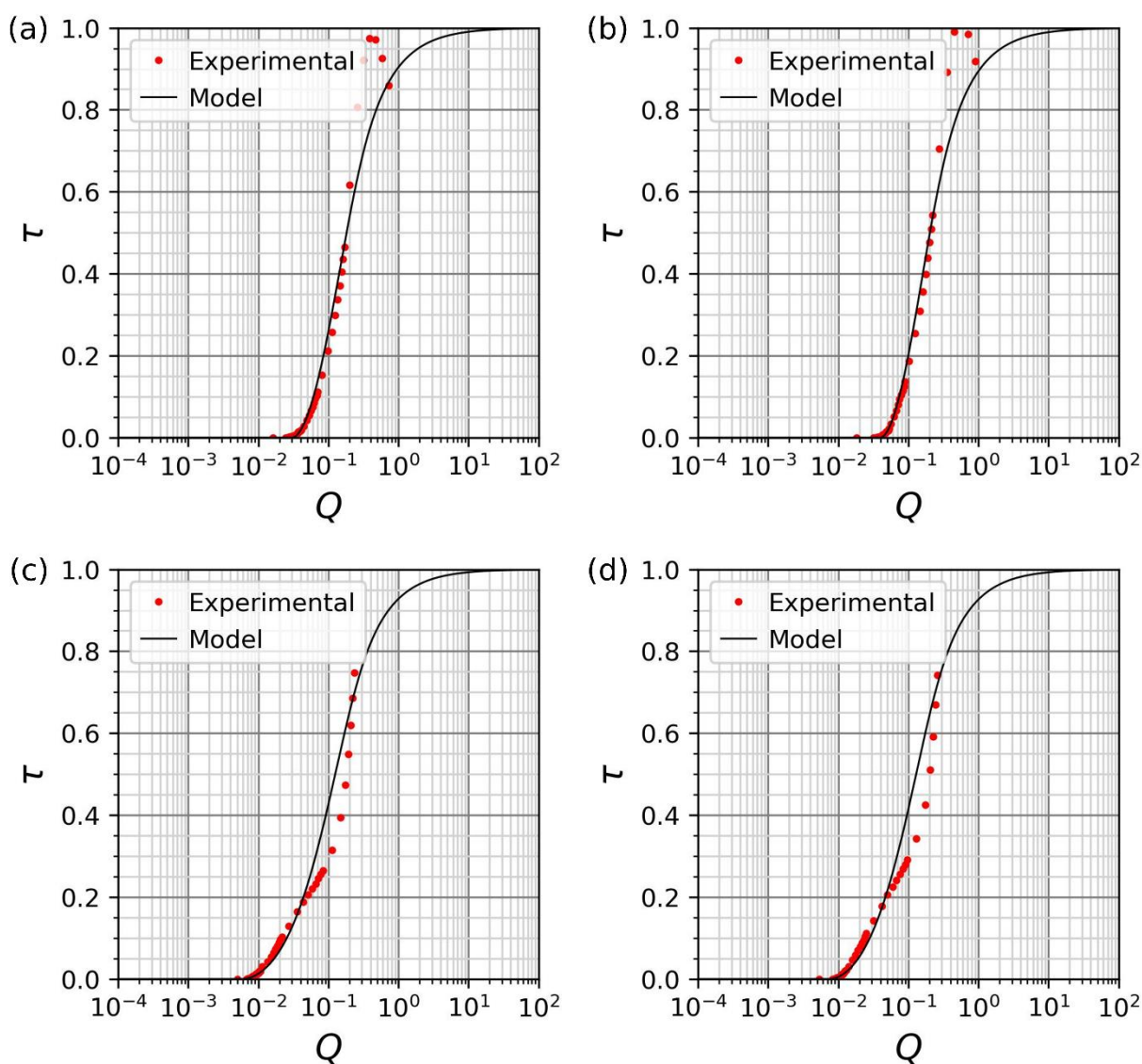
282   Figure S7: Examples of fits with (a-b) too much decrease in dq/dV in discharge and (c-d) too much
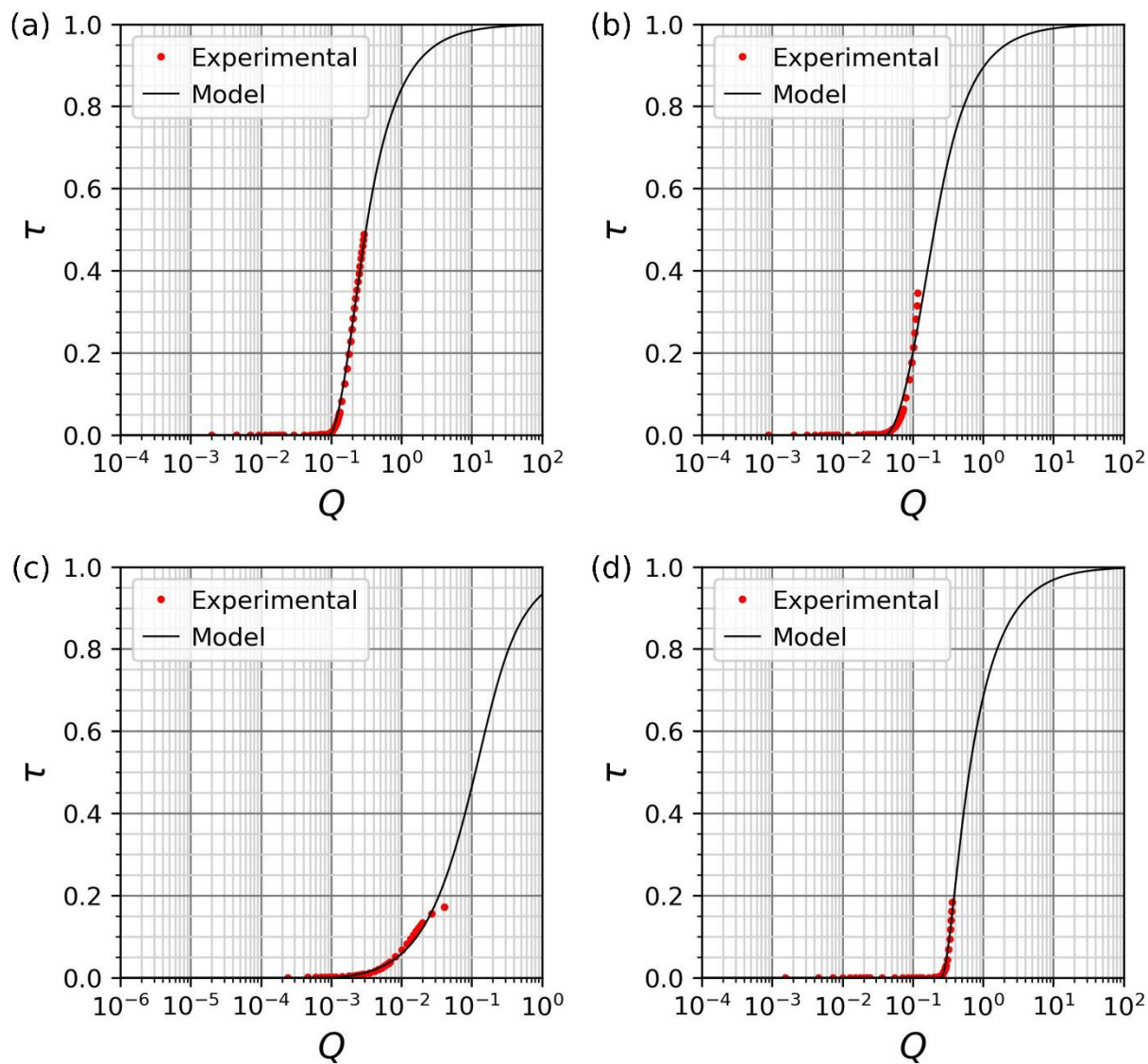283   increase in dq/dV in charge. Only NM9505 showed this error at its 4.15 V q-V plateau.

284

285   Figure S8: Examples of fits with not enough τ in order of decreasing τ. This occurs in (a, c) discharge and
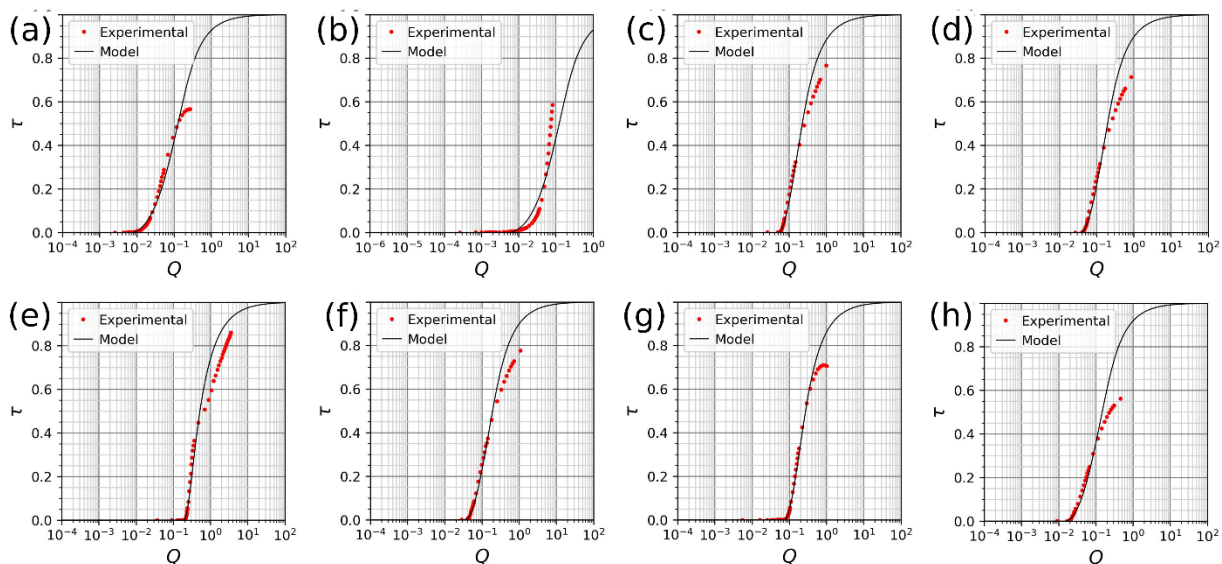286   (b, d) charge. All cells show this error at low SOC.

Figure S9: Examples of the highest fit error fits out of acceptable fits for (a-b) NMC640, (c-d) NMC811, (e-f) NM9505 with high resolution protocol, and (g-h) NM9505 with beta protocol. Both (a,c,e,g) discharge and (b, d, f, h) charge fits are shown.
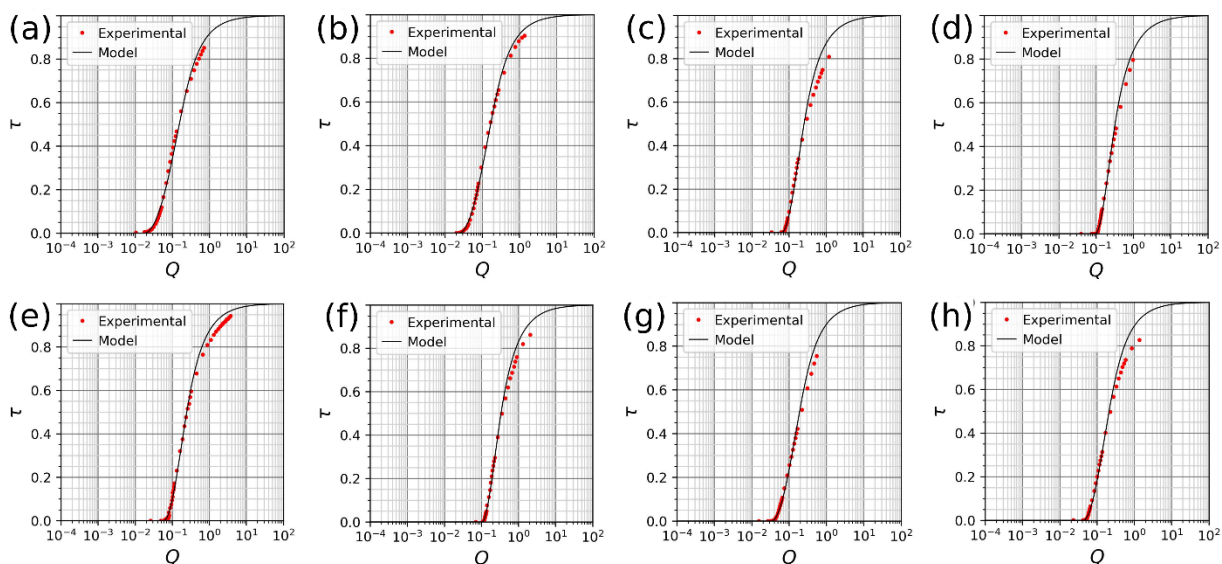

Figure S10: Examples of randomly selected, acceptable fits for (a-b) NMC640, (c-d) NMC811, (e-f) NM9505 with high resolution protocol, and (g-h) NM9505 with beta protocol. Both (a,c,e,g) discharge and (b, d, f, h) charge fits are shown.

References

1. S. Atlung, K. West, and T. Jacobsen, *J. Electrochem. Soc.*, **126**, 1311–1321 (1979).

2. J. Kim, S. Park, S. Hwang, and W.-S. Yoon, *J. Electrochem. Sci. Technol*, **13**, 19–31 (2022).

299

S23